Determining the Magnitude and Direction of Photoinduced Ligand Field Switching in Photochromic Metal−Organic Complexes: Molybdenum−Tetracarbonyl Spirooxazine Complexes

Michelle M. Paquette,[†] Brian O. Patrick,[‡] and Natia L. Frank*,[†]

[†]Department of Chemistry, P.O. Box 3065, University of Victoria, Victoria, British Columbia, Canada V8W 3 V6
[‡]Department of Chemistry, University of British Columbia, 2036 Main Mall, Vancouver, British Columbia, Canada V6T 1Z1

S *Supporting Information*

ABSTRACT: The ability to optically switch or tune the intrinsic properties of transition metals (e.g., redox potentials, emission/absorption energies, and spin states) with photochromic metal−ligand complexes is an important strategy for developing "smart" materials. We have described a methodology for using metal−carbonyl complexes as spectroscopic probes of ligand field changes associated with light-induced isomerization of photochromic ligands. Changes in ligand field between the ring-closed spirooxazine (SO) and ring-opened photomerocyanine (PMC) forms of photochromic azahomoadamantyl and indolyl phenanthroline-spirooxazine ligands are demonstrated through FT-IR, ^{13}C NMR, and computational studies of their molybdenum−tetracarbonyl complexes. The frontier molecular orbitals (MOs) of the SO and PMC forms differ considerably in both electron density distributions and energies. Of the multiple π^* MOs in the SO and PMC forms of the ligands, the LUMO+1, a pseudo-b_1-symmetry phenanthroline-based MO, mixes primarily with the $Mo(CO)_4$ fragment and provides the major pathway for $Mo(d) \rightarrow phen(\pi^*)$ backbonding. The LUMO+1 is found to be $0.2-0.3$ eV lower in energy in the SO form relative to the PMC form, suggesting that the SO form is a better π-acceptor. Light-induced isomerization of the photochromic ligands was therefore found to lead to changes in the energies of their frontier MOs, which in turn leads to changes in π-acceptor ability and ligand field strength. Ligand field changes associated with photoisomerizable ligands allow tuning of excited-state and ground-state energies that dictate energy/electron transfer, optical/electrical properties, and spin states of a metal center upon photoisomerization, positioning photochromic ligand−metal complexes as promising targets for smart materials.
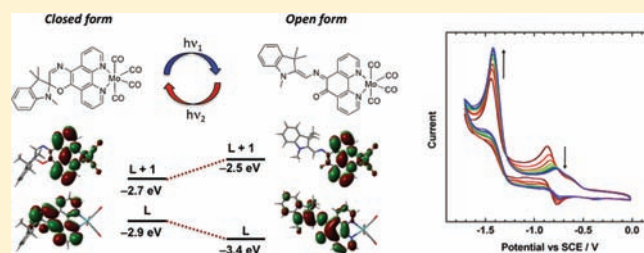
INTRODUCTION

Modulation of the physical properties of smart materials by light has led to the development of optical switches,[1] optoelectronics,[2] smart surfaces,[3] photoinduced shape-memory polymers,[4] peptides,[5] bionanodevices,[6] and molecular machines.[7] A versatile strategy toward the development of smart switching materials is the incorporation of photochromes[8] into hybrid inorganic−organic materials, in which reversible photoinduced isomerization of a photochrome leads to photoswitching of electrical, redox, magnetic, optical, or reactivity properties of a transition-metal complex or cluster.[9] Mediation of electronic communication (e.g., magnetic exchange, electron/energy transfer) between metal centers through a bridging photochromic unit,[9t,10] modulation of metal−photochrome sensitization processes in photochemically excited states,[9t,11] and exploitation of changes in photochrome volume or molecular geometry to perturb metal-based properties[9u,12] have been demonstrated. Manipulation of metal-based properties in photochromic metal−organics via changes in ligand field strength or symmetry has been recently explored in magnetically bistable cobalt−dioxolene redox isomeric complexes,[13] iron spin-crossover compounds,[14] and luminescent lanthanide complexes.[15]

Photochromic spirooxazines and spiropyrans have received great attention in recent years due to their potential applications in high-density optical storage, switching displays, communications systems, and ophthalmic lenses.[1d,16] Spirooxazines undergo UV-induced C−O bond cleavage of a ring-closed spirooxazine (SO) form ($\lambda_{max} \approx 350$ nm) to give the ring-opened photomerocyanine (PMC) form ($\lambda_{max} \approx 600$ nm) (Scheme 1). The PMC form is highly colored due to extended conjugation, with varying degrees of zwitterionic character dependent on both its structure and the surrounding medium.[17] Irradiation with visible light leads to C−O bond formation and regeneration of the closed SO form. Early work in our group investigated the irreversible metal complexation of photochromic spirooxazines in both the closed (SO) and open (PMC) states by incorporation of a phenanthroline into the oxazine moiety, leading to photoisomerizable ligands.[18] Investigation into the effect of metal complexation on the photochromic behavior of indolyl spirooxazines revealed large and tunable photoresponsivities associated with metal complexation compared to that of the parent photochrome.[18,19] Upon irradiation, changes in the electronic structure of the oxazine occur, which allow modulation of the
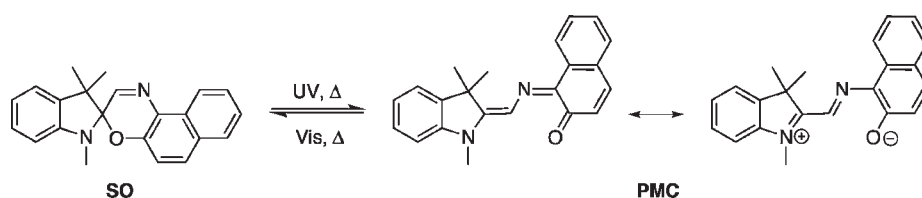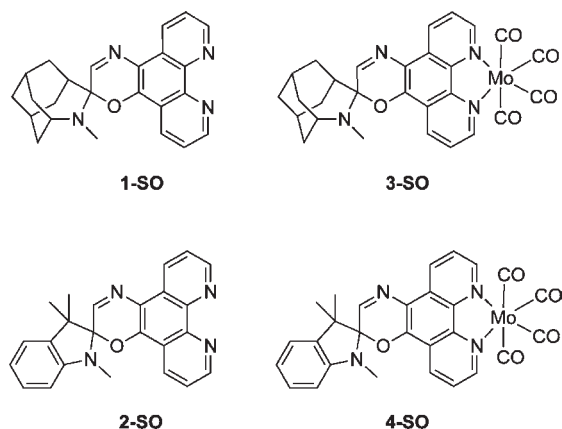
Scheme 1. Photoisomerization and Thermal Isomerization of Spiro[indoline-naphthoxazine] between Spirooxazine (SO) and Photomerocyanine (PMC) Forms

Chart 1.

1-SO   3-SO

2-SO   4-SO

ligand field about a metal center. Spectroscopic studies reveal changes in ligand field about the metal center arising from photoisomerization of the spirooxazine ligand.[19] Photochromic metal—organic complexes based on spirooxazines are therefore promising candidates for smart materials in which ligand photo-isomerization leads to modulation of the properties and reactivity of a bound metal center.

Current challenges associated with utilizing photoinduced ligand field changes in photochromic metal complexes for smart materials involve (1) improving the photochromic characteristics relevant to materials applications, such as quantum yield of photoisomerization, thermal stability of the metastable state, and wavelength of absorption/emission; (2) understanding the effect of inorganic—organic hybrid formation and metal com-plexation on the properties of the photochrome; and (3) evaluat-ing the effects of ligand photoisomerization on the properties of the metal center or inorganic component. Significant advances have been made over the years in understanding the structural features that dictate the physical properties of the various classes of photochromes. With the increasing importance of metal—organic photochromic systems to smart electronic, photonic, and biosensor applications,[9a,e,h,i,k,20] investigations into understand-ing the effect of ligand isomerization on the properties of the metal center are becoming increasingly important. In order to better design such systems, one needs to understand the effect of ligand photoisomerization on the electronic structure of the metal center. Critical to these studies is the evaluation of *both the magnitude and direction of ligand field change* (relative electro-negativity, π-acceptor and σ-donor ability) associated with ligand photoisomerization in a given photochromic class. To date, a generalized experimental method for evaluating the magnitude and direction of ligand field changes with ligand photoisomeriza-tion does not exist.

We have developed an experimental method for evaluating the changes in ligand field associated with spirooxazine photoisome-rization through the preparation and spectroscopic investigation of photochromic molybdenum—tetracarbonyl spirooxazine com-plexes, in which the CO group is utilized as a "reporter" group. Metal—carbonyl complexes have long been the gold standard for evaluating the relative ligand fields of different families of ligands due to the sensitivity of the carbonyl group to its electronic environment.[21] Herein we present the synthesis, spectroscopy, and computational studies for two phenanthroline-spirooxa-zine ligands, spiro[azahomoadamantane-phenanthrolinoxazine] (APSO, **1**) and spiro[indoline-phenanthrolinoxazine] (IPSO, **2**), and their respective molybdenum—tetracarbonyl complexes, Mo(CO)$_4$(APSO) (**3**) and Mo(CO)$_4$(IPSO) (**4**) (Chart 1). The ligand field strength of the SO and PMC forms of complexes **3** and **4** are investigated empirically with FT-IR and ^{13}C NMR spectroscopies, where the electronics of the carbonyl bond are analyzed by way of CO stretching frequencies and ^{13}C chemical shifts. Finally, a density functional theory (DFT) molecular orbital (MO) analysis and electrochemical studies are used to interpret the metal—ligand bonding interactions in these systems as a function of SO/PMC isomerization. For the spirooxazines examined, the SO form was found to be a better π-acceptor. An analysis of the spectroscopic features of photochromic molybde-num complexes allows for evaluation of the magnitude of ligand field changes associated with a particular photochromic ligand and can be generalized to other classes of photochromic ligands. Such studies provide insight into the modulation of electronic effects at the metal center due to photochromic ligands, critical for utilizing metal—organic photochromic complexes as optical switching components in light-actuated smart materials.

■ EXPERIMENTAL SECTION

Electronic Absorption Spectroscopy. Electronic absorption spectroscopy was performed at 300 K on $10^{-5}-10^{-6}$ M solutions prepared in spectroscopy grade solvents purchased from Caledon with an Agilent 8453 spectrometer. Extinction coefficients for the PMC $\pi-\pi^*$ transition were corrected for the %PMC form in a given solvent and at a given temperature as determined by ^{1}H NMR spectroscopy. For the determination of thermal isomerization kinetic parameters, sample solutions were transferred to 1 cm × 1 cm cuvettes, subjected to rapid uniform stirring, and exposed to steady-state multiline UV irradiation (λ_{ex} = 333.6−363.8 nm, power ≈ 30 mW) or single-line visible irradiation (λ_{ex} = 532 or 568 nm, power ≈ 45−50 mW) generated with a Spectra-Physics Stabilite 2018 mixed-gas Ar—Kr ion laser and directed through the sample cuvette at an angle perpendicular to the sampling beam with a Newport liquid light guide (LLG). A cuvette of acetone was placed between the sample and sampling beam to block irradiation from the spectrometer in the near-UV region (<300 nm). The rates of thermal return were determined in the absence of light after

10082

dx.doi.org/10.1021/ja109776z |*J. Am. Chem. Soc.* 2011, 133, 10081–10093

generation of a photostationary state. The absorbance kinetics of the PMC $\pi-\pi^*$ at the λ_{max} were fit to a monoexponential rate function by linear least-squares methods.

Cyclic Voltammetry. Cyclic voltammograms (CVs) were acquired with a BAS CV-50W voltammetric analyzer (with glassy carbon working, silver pseudoreference, and platinum counter electrodes). Sample solutions (10^{-4} M) in 0.1 M tetrabutylammonium tetrafluoroborate (TBA-TFB, Aldrich, 99%) CH_2Cl_2 or CH_3CN solutions were measured at a scan rate of 50 mV/s and temperature of 300 K. Spectroscopy grade, dry, and deoxygenated CH_2Cl_2 was acquired from an MBraun solvent purification system. Acetonitrile was distilled from CaH_2 under $N_{2(g)}$. Solvents were purged with $Ar_{(g)}$ for ≥ 5 min prior to acquiring CVs. Potentials were referenced to the $E_{1/2}$ value of the Fc^+/Fc redox couple of an internal ferrocene standard and are reported vs SCE (0.600 and 0.454 V vs Fc^+/Fc in 0.1 M TBA-TFB in CH_2Cl_2 and CH_3CN, respectively).[22]

Solution-State FT-IR. Saturated solutions were prepared in spectroscopy-grade CH_2Cl_2 obtained from an MBraun solvent purification system and filtered into a quartz solution sample cell. Spectra were acquired at 300 K with a Perkin-Elmer Spectrum One spectrometer with a CH_2Cl_2 background subtraction. Irradiation experiments were performed as described above for the electronic absorption spectroscopy experiments.

X-ray Crystallographic Analysis. A purple prism of $C_{28}H_{24}N_4O_5Mo \cdot C_7H_8$, having approximate dimensions of 0.04 mm × 0.12 mm × 0.22 mm, was mounted on a glass fiber. All measurements were made on a Bruker X8 APEX II diffractometer with graphite-monochromated Mo Kα radiation. The data were collected at a temperature of -100.0 ± 0.1 °C to a maximum 2θ value of 51.1°. Data were collected in a series of φ and ω scans in 0.50° oscillations with 60.0-s exposures. The crystal-to-detector distance was 36.00 mm. Of the 15 993 reflections that were collected, 5628 were unique (R_{int} = 0.034); equivalent reflections were merged. Data were collected and integrated using the Bruker SAINT[23] software package. The linear absorption coefficient, μ, for Mo Kα radiation is 4.78 cm^{-1}. Data were corrected for absorption effects using the multiscan technique (SADABS),[24] with minimum and maximum transmission coefficients of 0.932 and 0.981, respectively. The data were corrected for Lorentz and polarization effects. The structure was solved by direct methods.[25] The material crystallizes with one disordered molecule of toluene in the asymmetric unit. The disorder was modeled in two orientations, with a ratio of roughly 3:1 between the major and minor fragments. All non-hydrogen atoms were refined anisotropically. All hydrogen atoms were placed in calculated positions but were not refined. The final cycle of full-matrix least-squares refinement $[\Sigma w(F_o^2 - F_c^2)^2]$ on F^2 was based on 5628 reflections and 412 variable parameters and converged (largest parameter shift was 0.00 times its esd) with unweighted and weighted agreement factors of $R_1 = \Sigma||F_o| - |F_c||/\Sigma|F_o| = 0.044$ and $wR_2 = \{\Sigma[w(F_o^2 - F_c^2)^2]/\Sigma w(F_o^2)^2]\}^{1/2} = 0.074$. The standard deviation of an observation of unit weight $\{[\Sigma w(F_o^2 - F_c^2)^2/(N_o - N_v)]^{1/2}$, where N_o is the number of observations and N_v is the number of variables} was 1.03. The weighting scheme was based on counting statistics. The maximum and minimum peaks on the final difference Fourier map corresponded to 0.40 and -0.40 e^- $Å^{-3}$, respectively. Neutral atom scattering factors were taken from Cromer and Waber.[26] Anomalous dispersion effects were included in F_{calc};[27] the values for $\Delta f'$ and $\Delta f''$ were those of Creagh and McAuley.[28] The values for the mass attenuation coefficients are those of Creagh and Hubbell.[29] All refinements were performed using the Bruker AXS SHELXTL[30] crystallographic software package.

Computational Methods. Molecular geometries of the stationary points on the potential energy surface of the isomers of **1**−**4** were optimized with the Gaussian 03 software package[31] using density

functional theory (DFT)[32] with the B3LYP functional, consisting of Becke's three-parameter hybrid exchange functional[33] combined with the Lee−Yang−Parr correlation functional.[34] Ligand geometry optimizations were performed with the 6-31G(d,p) basis set, and Mo complex geometry optimizations were performed with the double-ζ effective core potential LANL2DZ basis set.[35]

Synthesis. *General.* All reagents were purchased from commercial sources and used without further purification. Spectroscopy-grade, dry, and deoxygenated toluene and pentane were acquired from an MBraun solvent purification system. Reactions were run under $N_{2(g)}$ or $Ar_{(g)}$ and worked up in air. ^{1}H NMR spectra were acquired with Bruker AC300, Bruker AC360, or AVANCE500 spectrometers, and spectra were calibrated to the solvent residual peaks (CDCl$_3$, 7.24 ppm for ^{1}H NMR; CD$_2$Cl$_2$, 5.32 ppm for ^{1}H NMR and 53.80 ppm for ^{13}C NMR). The ^{1}H NMR data reported are for samples that are thermally equilibrated at room temperature (300 K) in the absence of light irradiation in a given solvent. The preparations of spiro[azahomoadamantane-phenanthrolinoxazine] (**1**)[17] and spiro[indoline-phenanthrolinoxazine] (**2**)[13] have been previously reported. Mo complexes were prepared from Mo-$(CO)_4(pip)_2$, which was prepared from $Mo(CO)_6$ following a known procedure.[36]

Mo(CO)$_4$(APSO) (**3**). Mo(CO)$_4$(pip)$_2$ (83.9 mg, 0.222 mmol, 1.00 equiv) and **1** (84.8 mg, 0.221 mmol, 1.00 equiv) were stirred in toluene (15 mL) in the absence of light at ~300 K for 19 h. The resulting precipitate was filtered and washed with toluene to yield a dark purple powder (119 mg, 90% isolated yield). ^{1}H NMR (360 MHz, CD$_2$Cl$_2$) for PMC form: δ 10.27 (s, 1H), 9.23 (dd, J = 5.1, 1.6 Hz, 1H), 8.91 (dd, J = 4.9, 1.5 Hz, 1H), 8.83 (dd, J = 8.0, 1.7 Hz, 1H), 8.76 (dd, J = 8.3, 1.5 Hz, 1H), 7.56 (dd, J = 8.0, 5.1 Hz, 1H), 7.45 (dd, J = 8.4, 5.0 Hz, 1H), 5.09 (br t, J = 6.1 Hz, 1H), 3.86 (sept, J = 2.2 Hz, 1H), 3.61 (s, 3H), 2.2−1.8 (m, 12H) ppm. ^{1}H NMR (360 MHz, CD$_2$Cl$_2$) for SO form: δ 7.79 (s, 1H) ppm (as the SO form makes up only 2% of the total concentration of **3**, only the azomethine proton resonance can be unambiguously identified). ^{13}C NMR (90 MHz, CD$_2$Cl$_2$) for PMC form: δ 223.4, 223.3, 205.7, 182.8, 171.3, 154.3, 151.3, 148.4, 142.5, 136.0, 135.3, 131.6, 131.5, 129.5, 125.1, 124.8, 123.9, 66.0, 43.7, 34.1, 33.6, 32.0, 30.2, 26.6 ppm. IR (KBr): (C−O) 2006, 1889, 1859, 1816 cm^{-1}. ESI-MS: m/z (%) 598 (100) [M]$^+$. Anal. Calcd for $C_{28}H_{28}MoN_4O_5 \cdot (C_6H_5CH_3)_{0.5}$: C, 58.88; H, 5.02; N 8.72. Found: C, 57.98; H, 4.68; N, 7.92.

Mo(CO)$_4$(IPSO) (**4**). Mo(CO)$_4$(pip)$_2$ (126 mg, 0.333 mmol, 1.00 equiv) and **2** (126 mg, 0.331 mmol, 1.00 equiv) were stirred in toluene (15 mL) in the absence of light at ~300 K for 3 h. The resulting precipitate was filtered and washed with toluene to yield a blue microcrystalline powder (163 mg, 84% isolated yield). ^{1}H NMR (360 MHz, CD$_2$Cl$_2$) for PMC form: δ 10.28 (s, 1H), 9.27 (dd, J = 5.2, 1.7 Hz, 1H), 9.00 (dd, J = 5.0, 1.4 Hz, 1H), 8.81 (dd, J = 8.0, 1.6 Hz, 1H), 8.76 (br d, J = 8.4, 1H), 7.59 (dd, J = 8.0, 5.2 Hz, 1H), 7.56 (dd, J = 8.3, 5.0 Hz, 1H), 7.51 (ddd, J = 7.3, 1.2, 0.5 Hz, 1H), 7.46 (td, J = 7.6, 1.3 Hz, 1H), 7.35 (td, J = 7.6, 0.9 Hz, 1H), ~7.2 (m, 1H), 3.81 (br s, 3H), 1.90 (br s, 6H) ppm. ^{1}H NMR (360 MHz, CD$_2$Cl$_2$) for SO form: δ 9.39 (dd, J = 5.1, 1.5 Hz, 1H), 9.31 (dd, J = 5.0, 1.5 Hz, 1H), 9.11 (dd, J = 8.4, 1.5 Hz, 1H), 8.54 (dd, J = 8.3, 1.5 Hz, 1H), 7.94 (s, 1H), 7.78 (dd, J = 8.4, 5.0 Hz, 1H), 7.63 (dd, J = 8.3, 5.0 Hz, 1H), 7.25 (td, J = 7.6, 1.2 Hz, 1H), 7.15 (ddd, J = 7.2, 1.2, 0.6 Hz, 1H), 6.95 (td, J = 7.4, 0.9 Hz, 1H), 6.64 (br d, J = 7.7 Hz, 1H), 2.79 (s, 3H), 1.42 (s, 3H), 1.40 (s, 3H) ppm. ^{13}C NMR (125 MHz, CD$_2$Cl$_2$) for PMC and SO forms: δ 223.3, 223.1, 205.6, 205.4, 184.6, 154.9, 153.5, 153.5, 153.2, 151.2, 149.5, 148.5, 147.4, 146.5, 142.5, 140.1, 136.2, 135.8, 135.1, 132.1, 131.7, 131.6, 131.5, 131.3, 128.9, 128.8, 128.6, 128.4, 126.2, 125.4, 125.1, 125.0, 124.4, 124.4, 124.3, 123.2, 122.8, 122.0, 120.7, 120.4, 120.1, 111.3, 107.8, 107.6, 100.9, 52.5, 29.8, 28.1, 25.8, 25.7, 22.7, 20.8 ppm. IR (KBr): (C−O) 2008, 1893 (sh), 1889, 1873 (sh), 1868, 1858, 1850, 1841, 1837 (sh), 1829 cm^{-1}. ESI-MS: m/z (%) 594 (100) [M]$^+$. Anal. Calcd for $C_{28}H_{24}MoN_4O_5$: C, 56.76; H, 4.08; N 9.46. Found: C, 55.05; H, 3.69; N, 8.90.

10083

dx.doi.org/10.1021/ja109776z |*J. Am. Chem. Soc.* 2011, 133, 10081–10093

■ RESULTS AND DISCUSSION

Solution-State Behavior and Photochromism. Key solution-state properties of the two molybdenum complexes, **3** and **4**, and their respective parent ligands, **1** and **2**, were studied by ^{1}H NMR and electronic absorption spectroscopy. Spirooxazines undergo reversible thermal isomerization between SO and PMC forms to establish a thermal equilibrium ($K_T = [PMC]/[SO]$) between the two species. The thermal equilibrium can be shifted to a photoinduced equilibrium (i.e., a photostationary state) with steady-state UV or visible irradiation (Scheme 2). As the rate and equilibrium constants associated with the photoprocesses are dependent on experimental conditions (i.e., irradiation power, sample volume, etc.), only the thermal rate constants are reported in this study.

The thermal equilibrium constants, K_T, for **1**–**4** were determined by ^{1}H NMR spectroscopy in toluene and CH$_2$Cl$_2$ at 300 K. By calculating the ratio of the peak areas for the azomethine proton resonances of the PMC ($\delta \approx 10$ ppm) and SO ($\delta \approx 8$ ppm) forms, the equilibrium constants were obtained. From the values summarized in Table 1, it is evident that under the experimental conditions, the PMC form is the most stable for the azahomoadamantyl-based compounds, **1** and **3**, while the SO form is most stable for the indolyl-based compounds, **2** and **4**, consistent with the tendency of the azahomoadamantyl group to stabilize the PMC form.[17] For both the azahomoadamantyl and indolyl spirooxazines, the
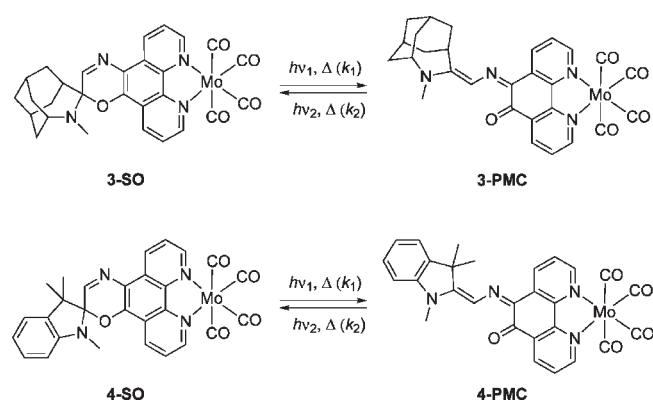
PMC form is significantly stabilized upon metal complexation, consistent with previous studies.[18,19] The PMC form is further stabilized in polar solvents for **1**–**4**.

Two major transitions are observed in the visible region of the electronic absorption spectra for the photochromic complexes: an intense band at ~550 nm for **3** and ~600 nm for **4** is assigned to a PMC-based $\pi-\pi^*$ transition, and a broad, less intense band at ~450 nm for **3** and ~500 nm for **4** is assigned to a metal-to-ligand (ML) Mo(d)→diimine(π^*) charge-transfer (CT) process. The absorption wavelengths (λ_{max}) and extinction coefficients (ε) for these bands are summarized in Table 1 for toluene and CH$_2$Cl$_2$ solutions of **1**–**4**. For the PMC $\pi-\pi^*$ absorption bands, a shift in λ_{max} is observed upon metal complexation, which is both ligand and solvent dependent. Upon complexation with Mo(CO)$_4$, the PMC $\pi-\pi^*$ transition of the ligand **2** exhibits a bathochromic shift in all solvents examined [Supporting Information (SI)]. Complexation of **2** to first-row transition metals has previously been shown to lead to bathochromic shifts,[18] consistent with the results observed for the Mo(CO)$_4$IPSO complex **4**. Ligand **1**, on the other hand, exhibits either a hypsochromic [554–546 nm (toluene)] or bathochromic shift [554–558 nm (CH$_2$Cl$_2$)] upon complexation, depending on solvent (SI). TD-DFT single point calculations performed on complexes **3** and **4** predict a small bathochromic shift in the PMC $\pi-\pi^*$ transition upon Mo complexation for both complexes in the gas phase (SI). Therefore, the solvent dependence found in complex **3** may be due to the sensitivity of PMC form excitation energies to the dielectric of the medium,[17] giving rise to the variation with solvent observed, consistent with the solvatochromic behavior of merocyanine dyes.[37] The extinction coefficients for the PMC $\pi-\pi^*$ transitions (ε_{PMC}) are solvent dependent and range from 40 000 to 90 000 M^{-1} cm^{-1} for **1**, **2**, and **4**, but are significantly lower for **3** (18 000 M^{-1} cm^{-1} in toluene and 6700 M^{-1} cm^{-1} in CH$_2$Cl$_2$). The MLCT bands observed for **3** and **4** were assigned by analogy with the Mo(CO)$_4$(phen) complex, which displays a MLCT band of similar energy and extinction coefficient (490 nm, 6160 M^{-1} cm^{-1} in benzene).[38]

Freshly prepared solutions of **4** exhibit a decrease in the PMC $\pi-\pi^*$ absorption band with time (SI), which suggests a shift in the SO–PMC equilibrium toward the PMC form in the solid state relative to solution. The absorbance intensities for **4** in CH$_2$Cl$_2$ were measured as a function of time after dissolution and are consistent with ≥50% PMC in the solid state, followed by equilibration to 6% PMC in toluene (12% PMC in CH$_2$Cl$_2$) in ~10 min. No analogous SO–PMC equilibration is observed for **3**, and, because the thermal equilibrium for **3** is shifted to >95% PMC

Scheme 2. Photoisomerization and Thermal Isomerization of Molybdenum–Tetracarbonyl Spirooxazine Complexes 3 and 4 between Spirooxazine (SO) and Photomerocyanine (PMC) Forms ($h\nu_1$ = UV, $h\nu_2$ = Visible)

Table 1. Absorption Wavelengths (λ_{max}, nm), Extinction Coefficients (ε, M^{-1} cm^{-1}), Thermal Equilibrium Constants (K_T),[a] % PMC Values, and Thermal Isomerization Rate Constants (k, ×10^{-3} s^{-1})[b] of 1–4 at 300 K

	toluene						CH$_2$Cl$_2$					
	λ_{max} (ε)	K_T (%PMC)	k_{vis}^{-1}	k_{UV}^{-1} (k_{dis})	k_1	k_2	λ_{max} (ε)	K_T (%PMC)	k_{vis}^{-1}	k_{UV}^{-1} (k_{dis})	k_1	k_2
1	555 (43000)[c]	1.2 (55)[c]	150	190	82[c]	68[c]	555 (60000)	11 (92)	56	–	51	4.7
2	581 (70000)[c]	0.02 (2)[c]	–	230	4.5[c]	230[c]	591 (81000)	0.06 (5)	–	740	42	700
3	465 (7400), 546 (18000)	>20 (>95)[d]	4.0	–	4.0[e]	–	465 (1500), 557 (6700)	50 (98)	3.4	–	3.3	0.067
4	511 (6900), 585 (88000)	0.06 (6)	34	(23)	1.9	32	476 (6600), 605 (62000)	0.14 (12)	14	(14)	1.7	12

[a] Determined by ^{1}H NMR spectroscopy in deuterated solvents. [b] Determined by electronic absorption spectroscopy. [c] Reference 17. [d] Compound **3** is minimally soluble in toluene, and the amount of SO form in solution, if any, cannot be determined within the ^{1}H NMR detection limits. [e] Assuming $k_1 \gg k_2$.
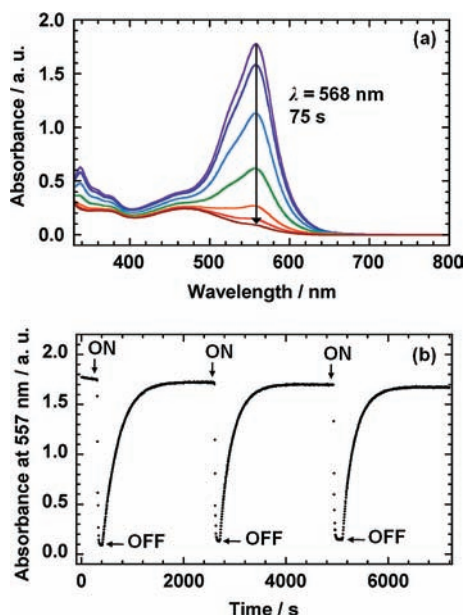
Figure 1. (a) Electronic absorption spectrum of a CH_2Cl_2 solution of **3** at ~300 K upon visible irradiation at 568 nm. (b) Kinetic profile of the absorbance intensity at the PMC $\pi-\pi^*$ λ_{max} value of 557 nm over three irradiation cycles.

Table 2. Redox Potentials (V vs SCE) for 1−4 in CH_2Cl_2 and CH_3CN at ~300 K^a

	E_{pc}		$E_{1/2}$	ΔE_p	i_a/i_c	E_{pa}	
	Red$_2$	Red$_1$				Ox$_1$	Ox$_2$
			CH_2Cl_2				
1	−1.63	−1.15	−1.10	0.080^b	0.70^b	0.79	1.08
2	−1.64	−0.84	−0.82	0.120	0.85	^{c}	^{c}
3^d	−1.42	−1.04	−1.01	0.085^e	0.80^e	0.89	
4^d	−1.44	−0.87	−0.82	0.105	0.76	0.83	
		(−0.78)^f	(−0.75)^f	(0.056)^f	(0.50)^f		
			CH_3CN				
1	−1.70	−1.26	−1.22	0.080	0.65	0.59	0.86
2	−1.71	−1.02	−0.99	0.060	2.60	0.86	1.07

^{a} Experimental conditions: electrolyte, 0.1 M TBA-TFB in deoxygenated CH_2Cl_2 or CH_3CN solution; scan rate, 50 mV/s; electrode configuration, glassy carbon working electrode, silver pseudoreference electrode, platinum counter electrode; referenced to the Fc^+/Fc redox couple and reported vs SCE. ^{b} If the first reduction wave is isolated, these values are $\Delta E_p = 0.160$ V, $i_a/i_c = 1.0$. ^{c} The oxidation processes for **2** in CH_2Cl_2 are not distinguishable; see SI. ^{d} Complexes **3** and **4** are sparingly soluble in CH_3CN, and CVs were only acquired in CH_2Cl_2. ^{e} If the first reduction wave is isolated, these values are $\Delta E_p = 0.059$ V, $i_a/i_c = 1.0$. ^{f} The first value listed is for the first time trace; the value in parentheses is for the last time trace.

form in solution (toluene, CH_2Cl_2), the complex must exist almost entirely in the PMC form in the solid state. The observed shift in SO−PMC equilibrium with dissolution is entirely consistent with the strong effect of medium dielectric on the structure and equilibrium constant (K_T) of ligand **2** over that of ligand **1** observed previously.[17]

Steady-state UV irradiation of solutions of **4** leads to an increase in the intensity of the PMC $\pi-\pi^*$ band, consistent with photoinduced ring-opening to the PMC form, and a simultaneous decrease in the intensity of the MLCT band. When irradiation is ceased, the PMC band decreases to its original intensity, but changes in the MLCT band are not reversible. This is evidence for the UV-induced decomplexation of the spirooxazine ligand, which is corroborated by both a permanent shift of the PMC $\pi-\pi^*$ λ_{max} to a lower wavelength after one irradiation/ thermal relaxation cycle and the appearance of free ligand signals in the ^1H NMR spectrum after UV irradiation. With subsequent UV irradiation cycles, the intensity of the $\pi-\pi^*$ band increases and decreases repeatedly without loss of intensity, which suggests that the spirooxazine ligand remains intact and photochromic after decomplexation. This behavior is observed in a range of solvents including toluene, acetone, MeOH, and CH_3CN (shown for a toluene solution in the SI). In CH_2Cl_2, however, the spirooxazine ligand appears to undergo both decomplexation and decomposition, as evidenced by the disappearance of the MLCT band with UV irradiation and a gradual decrease in the maximum absorbance intensity of the PMC band reached upon thermal relaxation after each irradiation cycle. Similar behavior with UV irradiation is observed for complex **3** (SI).

Upon steady-state visible irradiation (λ_{ex} = 568 nm), solutions of **3** and **4** exhibit a decrease in the intensity of the PMC $\pi-\pi^*$ absorption band, consistent with PMC→SO conversion (Figure 1a). The $\pi-\pi^*$ band returns gradually to its original intensity in the absence of light with monoexponential kinetics. This behavior repeats over sequential irradiation/thermal

reversion cycles with little change in the limiting absorbance intensities (Figure 1b), which indicates that the complexes are photoresponsive to visible irradiation without undergoing significant photodegradation.

Two thermal isomerization reactions can occur in thermally reversible spirooxazines: (1) SO→PMC isomerization with a rate constant k_1 and (2) PMC→SO isomerization with a rate constant k_2 (Scheme 2). The observed rate constant for thermal return from a photostationary state, k_{obs}, is defined as $k_{obs} = k_1 + k_2$.[39] This rate constant was determined by monitoring the time dependence of the absorbance intensity of the PMC $\pi-\pi^*$ transition at λ_{max} during (1) thermal equilibration toward the SO form after establishing a photostationary state with UV irradiation (k_{UV}^{-1}), (2) thermal equilibration toward the PMC form after establishing a photostationary state with visible irradiation (k_{vis}^{-1}), or (3) during thermal equilibration toward the SO form upon initial dissolution of a solid sample (k_{dis}). The kinetic parameters are summarized in Table 1. The rate constants of SO→PMC isomerization, k_1, are similar for both **1** and **2**, but the rate constants for the reverse isomerization, k_2, are an order of magnitude lower for the azahomoadamantyl spirooxazine ligand **1** than for the indolyl spirooxazine ligand **2**. In general, the rate constants for the molybdenum complexes are an order of magnitude lower than those for their respective free ligands, consistent with the effect of complexation of **2** with first-row transition metal ions.[18]

To summarize, **4** exists as ≥50% PMC and **3** as ~100% PMC in the solid-state samples, while in solution **4** exists predominantly in the SO form and **3** exists predominantly in the PMC form. Both of the Mo complexes appear to be sensitive to decomplexation by UV light but are photoresponsive and photochemically stable upon irradiation with visible light. In the study of these systems, we can therefore efficiently experimentally monitor either (a) the thermal SO→PMC equilibration of **3** after

10085

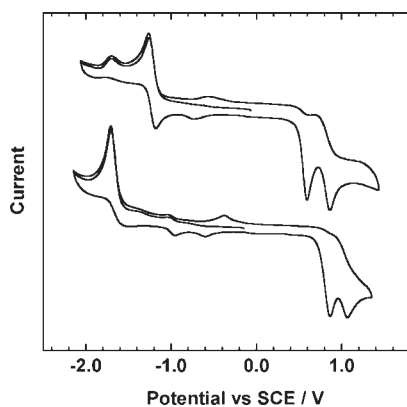dx.doi.org/10.1021/ja109776z |*J. Am. Chem. Soc.* 2011, 133, 10081−10093

Figure 2. CVs of **1** (top) and **2** (bottom) in deoxygenated 0.1 M TBA-TFB CH$_3$CN solutions at 300 K (electrode configuration, glassy carbon working electrode, silver pseudoreference electrode, platinum counter electrode; scan rate, 50 mV/s; referenced to the Fc$^+$/Fc redox couple and reported vs SCE).
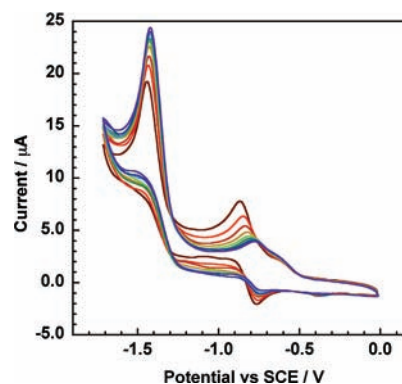

Figure 3. CV of **4** in a deoxygenated 0.1 M TBA-TFB CH$_2$Cl$_2$ solution at 300 K over time (electrode configuration, glassy carbon working electrode, silver pseudoreference electrode, platinum counter electrode; scan rate, 50 mV/s; referenced to the Fc$^+$/Fc redox couple and reported vs SCE).

a photostationary state is established with visible irradiation (where this photostationary state is nearly 100% SO form, and the system can be monitored from ~100% SO form to ~100% PMC form) or (b) the thermal PMC→SO equilibration of **4** immediately following dissolution (where ~50% PMC form is converted to ~10% PMC form over time).

Cyclic Voltammetry. The electrochemical behavior of the spirooxazine ligands was investigated by cyclic voltammetry. CVs of **1** and **2** were acquired in deoxygenated 0.1 M TBA-TFB CH$_2$Cl$_2$ and CH$_3$CN solutions at 300 K at a scan rate of 50 mV/s. All potentials were referenced to the Fc$^+$/Fc redox couple and reported vs SCE. The relevant electrochemical data are summarized in Table 2, and representative CVs of **1** and **2** in CH$_3$CN are shown in Figure 2 (the CVs of **1** and **2** in CH$_2$Cl$_2$ are shown in the SI).

In acetonitrile, two irreversible oxidation processes (Ox$_1$ and Ox$_2$) are observed for each of the ligands, with anodic peak potentials, E_{pa}, occurring between 0.6 and 1.1 V. In methylene chloride, only ligand **1** exhibits these two oxidation processes (SI). Two notable reduction processes are also observed in each of the ligands. For **1** in CH$_2$Cl$_2$, a major quasireversible reduction wave (Red$_1$) is observed with half-wave potential $E_{1/2}$ = −1.10 V (ΔE_p = 0.080 V, i_a/i_c = 0.70), and a second minor irreversible process (Red$_2$) is observed with cathodic peak potential E_{pc} = −1.63 V. For **2** in CH$_2$Cl$_2$, a minor quasireversible reduction process (Red$_1$) is observed with $E_{1/2}$ = −0.82 V (ΔE_p = 0.120 V, i_a/i_c = 0.85), and a major irreversible process (Red$_2$) is observed with E_{pc} = −1.64 V. Two additional peaks are observed between 0 and −1.0 V for both **1** and **2** after either anodic or cathodic sweeps, suggesting some decomposition of the products of either reduction or oxidation.

For electrochemically reversible processes, the peak current is proportional to the concentration of electrochemically active species in solution.[40] Even though the reduction processes for spirooxazines **1** and **2** are quasireversible or irreversible, we have tentatively assigned them to SO- or PMC-based processes on the basis of the relative concentrations of these species in solution. From ^{1}H NMR spectroscopy, it was determined that the majority of **1** exists in the PMC form (95 and 92% in CD$_3$CN and CD$_2$Cl$_2$, respectively) and the majority of **2** exists in the SO form (94 and 95%, in CD$_3$CN and CD$_2$Cl$_2$, respectively).[41] We can therefore

reasonably assign the major reduction process (Red$_1$) for **1** to a PMC-based process and the reduction process for **2** (Red$_2$) to a SO-based process. We may also more tentatively assign the minor reduction process (Red$_1$) for **2** to a PMC-based process. This assignment is consistent with 5% PMC species in solutions of **2** and the existence of an analogous reduction process in solutions of **1**, in which the PMC form is the major species in solution. Following similar reasoning for **1** and assigning the second reduction (Red$_2$) to a SO-based process may not be appropriate since the peak corresponding to Red$_2$ has a fairly high peak current relative to that of Red$_1$, and this may not be consistent with the SO species being present in only 5−8% in solution. This peak may in fact be due to a second reduction of the PMC species, which would be consistent with the lower i_a/i_c observed for the first reduction process after cycling through the second reduction process at more negative potentials.

The electrochemical behavior of the Mo complexes was investigated by cyclic voltammetry, and the data are summarized in Table 2. Complexes **3** and **4** are sparingly soluble in CH$_3$CN, and CVs of the complexes were therefore only acquired in solutions of CH$_2$Cl$_2$ with 0.1 M TBA-TFB. The electrochemical behavior of the complexes is analogous to that of the free ligands. Upon metal complexation, some of the reduction peaks are shifted to slightly more positive potentials, and the first reduction process (Red$_1$) exhibits greater reversibility. Again the electrochemical features can be tentatively assigned to SO- or PMC-based processes. The ^{1}H NMR spectra of the complexes indicate that, upon thermal equilibration in CD$_2$Cl$_2$ at 300 K, **3** exists as 98% PMC form, and the major reduction process observed at $E_{1/2}$ = −1.01 V is assigned to a PMC species. In solutions of **4**, which exists as 12% PMC in CD$_2$Cl$_2$ at 300 K, the system slowly equilibrates from the PMC form (≥50%) to the SO form (12%) over time (vide supra). The changes observed in the CV of a freshly dissolved sample over time, shown in Figure 3, are informative in assigning the reduction processes. Here, the cathodic peak current for the first reduction process decreases over time, and E_{pc} shifts from −0.87 to −0.77 V, while a peak at a more positive potential of −0.65 V grows in with the presence of an isosbestic point. The anodic peak current for this same reduction process also decreases over time, with a small shift in voltage (−0.76 to −0.73 V) leading to a decrease in ΔE_p for the process from 0.105 to 0.056 V. The peak current for the second
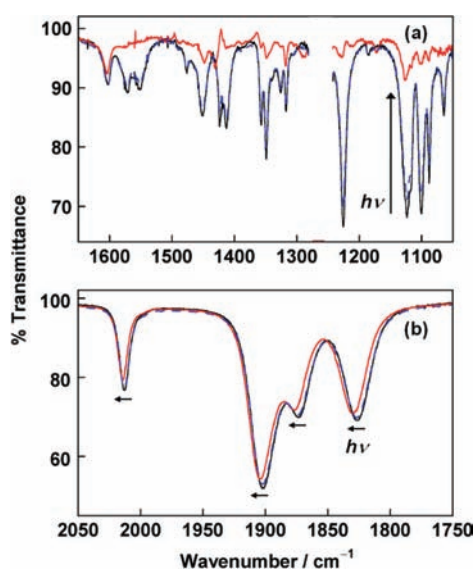
Figure 4. FT-IR spectrum of **3** in CH_2Cl_2 at ~300 K, illustrating spectral features in the fingerprint (a) and carbonyl stretching (b) regions before irradiation (black lines), immediately after 5 min of visible irradiation (λ_{ex} = 568 nm) (red lines), and after 17 min in the absence of light (blue lines). The gap at ~1275 cm^{-1} is due to a solvent background correction.

reduction process at $E_{pc} = -1.44$ V increases over time, with no associated shift in peak position. The changes in the relative peak currents for the two main reduction processes support the assignment of the first and second reduction processes to PMC- and SO-based processes, respectively, since the direction of change for the peak intensities corresponds with the expected PMC→SO isomerization upon dissolution. By extension, these observations also support the analogous peak assignments made above for the free ligands. The shift in E_{pc} and isosbestic behavior for what is assigned as a PMC-based reduction process suggests the formation of different electrochemically active species in solution over time and may be due to changes in aggregation or hydrogen bonding of the PMC species, or thermal isomerization to a different population of PMC isomers (i.e., where the three central bonds of the conjugated azomethine bridge have different *cis/trans* conformations). Evidence for the existence of multiple PMC isomers in solution for the Mo—spirooxazine complexes has been observed via ^1H NMR spectroscopy but not UV/vis electronic absorption spectroscopy (SI).

FT-IR Spectroscopy of Mo Complexes. Solution FT-IR spectra of a sample of **3** were acquired in CH_2Cl_2 at 300 K with and without irradiation. Spectra were acquired before irradiation, immediately after 5 min of irradiation with visible light (λ_{ex} = 568 nm) to monitor the spectral changes upon PMC→SO photoisomerization, and 17 min after the light was removed to monitor the spectral changes upon SO→PMC thermal isomerization (Figure 4). Upon PMC→SO photoisomerizaton, large spectral changes occur in the fingerprint region (Figure 4a), while the peaks in the CO stretching region shift to higher energies by 1−4 cm^{-1} (Figure 4b). These spectral changes are reversible following SO→PMC thermal isomerization, as evident from the return of the FT-IR spectrum to its original appearance after >15 min in the absence of light. Because **3** initially exists as 98% PMC form in CD_2Cl_2 at 300 K (Table 1) and the solution becomes essentially colorless after visible irradiation (SI), it may

Table 3. Energies (cm^{-1}) of CO Stretching Vibrational Modes of 3 and 4 in CH_2Cl_2 at 300 K^a

	B_2	A_1^1	B_1	A_1^2
		3		
SO	1830.0	1877.1	1904.3	2014.4
PMC	1826.6	1873.4	1902.0	2013.1
$\Delta\nu_{SO-PMC}$	3.4	3.7	2.3	1.3
		4		
SO	1831.5	1878.8	1905.4	2015.0
PMC	1830.0	1877.3	1904.4	2014.5
$\Delta\nu_{SO-PMC}$	1.5	1.5	1.0	0.5

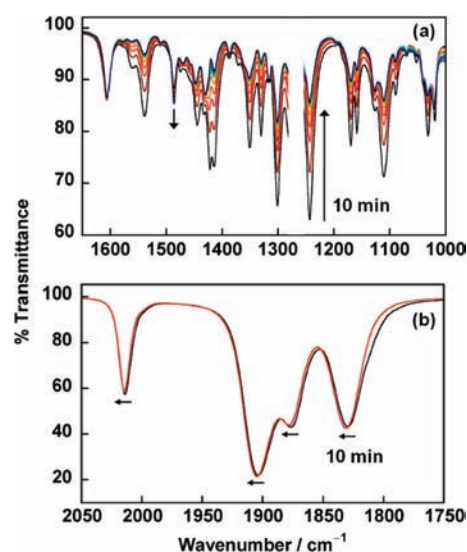^{a} Vibrational modes were assigned assuming pseudo-C_{2v} symmetry; see ref 42.

Figure 5. FT-IR spectrum of a freshly dissolved sample of **4** in CH_2Cl_2 at ~300 K over the course of 10 min, illustrating spectral changes in the fingerprint (a) and carbonyl stretching (b) regions upon PMC→SO thermal isomerization. The gap at ~1275 cm^{-1} is due to a solvent background correction.

be concluded that the complex converts from ~100% PMC form to ~100% SO form upon visible irradiation in CH_2Cl_2. The energies of the CO stretching vibrational modes determined before and after irradiation may therefore be assigned to the PMC or SO forms of the complex, respectively, as summarized in Table 3. Greater changes were observed in Nujol and KBr (SI), but due to band overlap and uncertainties in the ratio of SO/PMC after irradiation, the solution data in methylene chloride were chosen for analysis.

The FT-IR spectrum of a sample of **4** in CH_2Cl_2 at 300 K was monitored over time shortly after dissolution of the solid sample to observe the spectral changes occurring upon PMC→SO thermal isomerization (Figure 5). The observed changes are similar to those described above for **3**: the majority of the peaks in the fingerprint region decrease in intensity with some shifting (Figure 5a), while the peaks in the CO stretching region shift to higher energies by 0.5−1.5 cm^{-1} (Figure 5b). Although the direction of the experimental shifts for the CO peaks is the same for both **3** and **4** upon PMC→SO isomerization, the magnitude of these shifts is approximately half in the case of **4**. As **4** converts

Table 4. ^{13}C NMR Chemical Shifts (ppm) for the Carbonyl Groups of 3 and 4 in CD_2Cl_2 at 300 K

	$\delta_{CO(ax)}$	$\delta_{CO(eq)}$	
	4^a		
SO	205.44^c	223.14	223.26
PMC	205.59^c	223.26^d	223.34
$\Delta\delta_{PMC-SO}$ (Hz)	18.9	15.1	10.1
	3^b		
SO	—	—	—
PMC	205.73^c	223.29	223.41

^{a} Acquired at 90.56 MHz. ^{b} Acquired at 125.77 MHz. ^{c} Peak slightly broad; two peaks unresolved. ^{d} Assigned under the assumption that a second PMC peak is masked by the SO peak at 223.26 ppm.

Table 5. Crystal Data and Refinement Parameters for 3-PMC

formula	$C_{28}H_{28}MoN_4O_5 \cdot C_6H_5CH_3$
FW/g mol^{-1}	684.59
space group	$P\bar{1}$
a/Å	7.8137(8)
b/Å	9.9057(11)
c/Å	14.0837(16)
α/°	84.895(5)
β/°	77.368(5)
γ/°	81.828(5)
V/Å^3	3178.6(2)
D_{calcd}/g cm^{-3}	1.482
Z	2
T/°C	-100 ± 0.1
λ/Å	0.71073
μ (Mo Kα)/cm^{-1}	4.78
$R_1(F^2)$, wR_2 $(F^2)^a$	0.031, 0.074

^{a} $R_1 = \Sigma||F_o| - |F_c||/\Sigma|F_o|$, $I > 2\sigma I$.

from ~50% to ~10% PMC form over the course of the experiment, whereas **3** converts from ~100% to ~0% PMC form, the relative magnitudes of the shifts may be indicative of similar ligand field changes in both complexes, if it is assumed that their force constants are equivalent.

In FT-IR spectroscopy of metal—carbonyl complexes, higher energy CO stretching vibrational modes are associated with higher CO bond orders. The Cotton—Kraihanzel force constants, which can be calculated from the energies of the CO vibrational modes, most accurately parallel CO bond orders and take into account the $CO(\sigma) \rightarrow M(d)$ and $M(d) \rightarrow CO(\pi^*)$ interactions.[42,43] The energies of the modes yield useful semi-quantitative bonding information, particularly in the comparison of compounds of the same structure (e.g., only cis-$M(CO)_4(LL)$ complexes) and the same ligand type (e.g, only diimine ligands). In the Mo complexes **3** and **4**, four CO stretching modes are observed (Figures 4 and 5), as expected for six-coordinate, cis-tetracarbonyl complexes.[42] Each of these modes is shifted to higher energy in the SO form of the spirooxazine ligand relative to the PMC form (Table 3). The values of $\Delta\nu_{SO-PMC}$ are small but on the same order of magnitude as typically observed between $M(CO)_4(NN)$ complexes with different diimine ligands[44] (e.g., $Mo(CO)_4(bpy)$ and $Mo(CO)_4(phen)$ in CH_2Cl_2 or $CHCl_3$ show energy differences of 0—3 cm^{-1} for the four carbonyl stretching modes).[44d,f] Higher energy vibrational modes imply higher CO bond orders, which indicate less $M(d) \rightarrow CO(\pi^*)$ backbonding, which in turn reveals greater $M(d) \rightarrow phen(\pi^*)$ backbonding. Therefore, the FT-IR results indicate that the SO form behaves as a stronger π-acceptor than the PMC form.

^{13}C NMR Spectroscopy of Mo Complexes. ^{13}C NMR spectra of **3** and **4** were acquired in CD_2Cl_2 at 300 K, and the chemical shifts for the carbonyl groups are tabulated in Table 4. In both complexes, two sets of carbonyl resonances are observed: a first set at ~223 ppm assigned to the equatorial carbonyl groups (CO_{eq}), and a second set at ~205 ppm assigned to the axial carbonyl groups (CO_{ax}) (SI). In the set of CO_{eq} resonances for **4**, two intense peaks at 223.14 and 223.26 ppm and a less intense peak at 223.34 ppm are observed. The more intense peaks can be assigned to the SO form and the less intense one to the PMC form (as **4** exists as 12% PMC form from ^1H NMR data, Table 1). It is plausible that a second less intense peak is masked by the peak at 223.26 ppm and represents a second PMC-based CO_{eq} signal. The PMC-based resonances are more downfield than the SO-based resonances, and the differences between the chemical shifts of the two sets of signals, $\Delta\delta_{PMC-SO}$, are 15.1 Hz

(223.26−223.14 ppm) and 10.1 Hz (223.34−223.26 ppm). In the set of CO_{ax} resonances for **4**, only one intense and one weak peak are observed, at 205.44 and 205.59 ppm, respectively. Both of these peaks are more intense than those of the CO_{eq} groups, as each comprises two overlapping ^{13}C resonances from two axial carbonyl groups, consistent with pseudo-C_{2v} symmetry of the complex. The value of $\Delta\delta_{PMC-SO}$ is 18.9 Hz for the axial carbonyl groups, with the signal attributed to the PMC form further downfield. Although a ^{13}C NMR spectrum was also acquired for complex **3**, it was not useful for comparing chemical shifts between SO and PMC species since this complex exists as 98% PMC form in CD_2Cl_2 (Table 1).

In the ^{13}C NMR experiment, a linear relationship between the chemical shifts of the carbonyl groups and the Cotton—Kraihanzel CO stretching force constants exists for a number of systems.[45] An upfield ^{13}C chemical shift can be correlated with higher force constants and, by extension, higher energy CO vibrational modes and higher bond orders. In the Mo—tetracarbonyl spirooxazine complexes, the carbonyl chemical shifts were found to be more upfield in the SO form than in the PMC form (Table 4). Again, the $\Delta\delta_{PMC-SO}$ values are small but are on the same order of magnitude expected for $M(CO)_x$-$(L)_y$ complexes with different ligands, L.[45b] Thus, the ^{13}C NMR results reveal that the SO form is a stronger π-acceptor, consistent with the FT-IR results.

Structural Analysis of $Mo(CO)_4(APSO)$ (3). Purple prismatic crystals of **3**-PMC suitable for X-ray diffraction analysis were isolated from toluene. Crystal data and refinement parameters for **3**-PMC are summarized in Table 5. The complex crystallized in the triclinic $P\bar{1}$ space group with one disordered toluene solvate molecule per metal complex and two equivalent molecules per unit cell ($Z = 2$).

The molecular structure of **3**-PMC is shown in Figure 6, and selected bond lengths and angles are tabulated in Table 6. The geometrical parameters of the ligand in **3**-PMC are equivalent, within experimental error (0.02−0.03 Å), to those of the parent ligand, **1**-PMC.[17] The torsional angles N4—C14—C13—N3, C14—C13—N3—C6, and C13—N3—C6—C5 of **3**-PMC are 174.71°, 171.79°, and 5.42°, respectively, which indicates a nearly planar $trans$-$trans$-cis (or "TTC") conformation about the central conjugated azomethine bridge. This suggests that the TTC
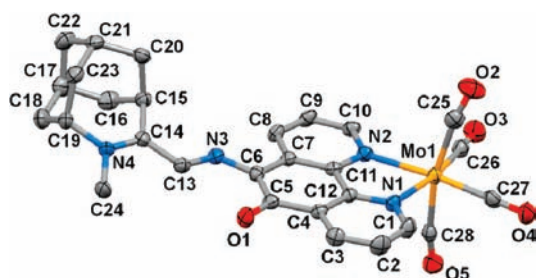
Figure 6. Molecular structure of **3**-PMC. Thermal ellipsoids are shown at the 50% probability level, and hydrogen atoms and toluene solvate molecules are omitted for clarity.

Table 6. Selected Bond Lengths and Angles for 3-PMC

bond lengths/Å		angles/°	
N4—C14	1.324(3)	N1—Mo1—C25	97.08(9)
C14—C13	1.430(3)	N1—Mo1—C28	92.63(8)
C13—N3	1.315(3)	N1—Mo1—C26	169.74(8)
N3—C6	1.344(3)	N1—Mo1—C27	99.75(9)
C6—C5	1.445(3)	N2—Mo1—C25	96.65(9)
C5—O1	1.236(3)	N2—Mo1—C28	94.71(8)
C1—N1	1.337(3)	N2—Mo1—C26	96.91(8)
C10—N2	1.333(3)	N2—Mo1—C27	172.58(8)
N1—Mo1	2.2450(19)	N1—Mo1—N2	72.90(7)
N2—Mo1	2.2412(19)	C25—Mo1—C28	166.82(10)
Mo1—C25	2.017(3)	C26—Mo1—C27	90.41(10)
Mo1—C28	2.050(3)	Mo1—C25—O2	170.2(2)
Mo1—C26	1.946(2)	Mo1—C28—O5	169.8(2)
Mo1—C27	1.944(3)	Mo1—C26—O3	177.8(2)
C25—O2	1.153(3)	Mo1—C27—O4	179.2(2)
C28—O5	1.140(3)	N4—C14—C13—N3	174.71
C26—O3	1.166(3)	C14—C13—N3—C6	171.79
C27—O4	1.167(3)	C13—N3—C6—C5	5.42

isomer is the most stable form in the solid state, as was found for the free ligand.[17] The bond lengths for the three bonds in the azomethine bridge, C14—C13 [1.430(3) Å], C13—N3 [1.315(3) Å], and N3—C6 [1.344(3) Å], demonstrate predominantly single-bond, double-bond, and single-bond character, respectively, when compared to average single and double bond lengths extracted from the Cambridge crystallographic database [C—C = 1.460(15) Å, C=C = 1.360(20) Å; C—N = 1.376(11) Å, C=N = 1.279(8) Å; N—C = 1.376(11) Å, N=C = 1.279(8) Å].[46] This bond length alternation pattern indicates that, in the Mo complex **3**-PMC, as in the free ligand **1**-PMC, the zwitterionic resonance form contributes more significantly to the PMC structure than does the quinoidal form (Scheme 1).

Crystallographic features relevant to the Mo(CO)$_4$ core of the complex are consistent with those observed in Mo(CO)$_4$-(phen).[47] Complex **3**-PMC has a distorted pseudo-octahedral geometry around the Mo center. The N1—Mo1—N2 angle is considerably less than 90° at 72.90(7)°, and the axial CO groups bend away from the diimine ligand to give a C25—Mo1—C28 angle of 166.82(10)°. The Mo—C and C—O bond lengths associated with the axial CO groups are respectively longer and shorter than those of the equatorial CO groups, consistent with greater Mo(d)→L(π*) backbonding between the diimine ligand and the axial CO groups. Additionally, the Mo—C and C—O bond lengths differ between the two axial CO groups. While the Mo1—C25 bond length is 2.017(3) Å with a C25—O2 bond length of 1.153(3) Å, the Mo1—C28 bond length of 2.050(3) Å is slightly longer with a decreased C—O bond length (C28—O5 = 1.140(3) Å). This is in contrast to the equivalent M—C and C—O bond lengths associated with the equatorial CO groups of 1.946(2)/1.944(3) Å and 1.166(3)/1.167(3) Å, respectively.

Examination of the crystal packing of **3**-PMC reveals that the molecules pack head-to-tail to form a network of intermolecular C—H···O interactions between the carbonyl oxygen atoms and phenanthroline C—H atoms (O3···H—C9 2.48 Å, and O2···H—C2 2.60 Å). In addition, short contacts between the phenolate oxygen and homoadamantyl C—H are observed (O1···H—C24 2.70 Å) (Figure 7). Both equatorial CO groups take part in intermolecular O···H interactions with neighboring PMC molecules (O3···H—C9 2.48 Å, O4···H—C19 2.56 Å, and O4···H—C24 2.52 Å), whereas the axial C25—O2 group with the longer C—O bond length of 1.153(3) Å is involved in an interaction with a nearby PMC hydrogen atom (O2···H—C2 2.60 Å), while the second axial CO group is not. This suggests that the bond length asymmetry observed for the axial CO groups may be due to solid-state intermolecular interactions rather than intrinsic electronic effects.

DFT Frontier MO Analysis. Molecular geometries of stationary points on the ground-state potential energy surfaces of spirooxazines **1**—**4** were optimized at the DFT/B3LYP level of theory[32−34] using the Gaussian 03 software package.[31] In the SO form of the spirooxazines, the chirality of the spiro carbon leads to two possible enantiomers, and in this work the (*R*)-enantiomer was arbitrarily chosen for computation. In the PMC form of the spirooxazines, the possibility of a predominantly *trans* or *cis* configuration about each of the three partial double bonds in the central conjugated azomethine bridge leads to eight possible stable isomers. Geometry optimizations were performed on the TTC isomer since it is known to be the most thermodynamically stable in nearly all spirooxazine-based PMCs,[48] and both **1** and **3** have been found to crystallize in this form.[17] Ligand geometries were optimized using the 6-31G(d,p) basis set. The B3LYP/6-31G(d) level of theory has successfully reproduced experimental geometries of the SO form of spirooxazines, except in some cases for the C$_{spiro}$—O bond length.[17,48a,49]

The three lowest-lying unoccupied π* MOs for the SO and PMC forms of **1** and **2** are shown in Figure 8. For discussion, the two lowest-lying π* MOs for phenanthroline,[50] which are close in energy and have b_1 and a_2 symmetries, are also shown (occupied MOs are shown in the SI). The closed form of ligand **1** (**1-SO**) exhibits significant differences in the form and energies of the three lowest unoccupied molecular orbitals, the LUMO, LUMO+1, and LUMO+2, arising from differential mixing of the oxazine and phen orbitals. The character of the frontier unoccupied MOs can be understood by separately considering the phenanthroline fragment and the remaining spirooxazine fragment.[51] In the phenanthroline fragment, the a_2 MO has larger orbital coefficients at the 5- and 6-positions than the b_1 MO, leading to greater mixing of the oxazine with the phen(a_2) MO fragment relative to the phen(b_1) fragment. While the LUMO+1 orbital is phenanthroline based and of pseudo-b_1 symmetry in analogy to the phen(b_1) orbital, the LUMO and LUMO+2 arise from mixing of the phen(a_2) and oxazine orbitals. In both forms, the LUMO+1 is essentially phen-based and can be assigned pseudo-b_1 symmetry by analogy with phen, assuming pseudo-C_{2v} symmetry for the complex.
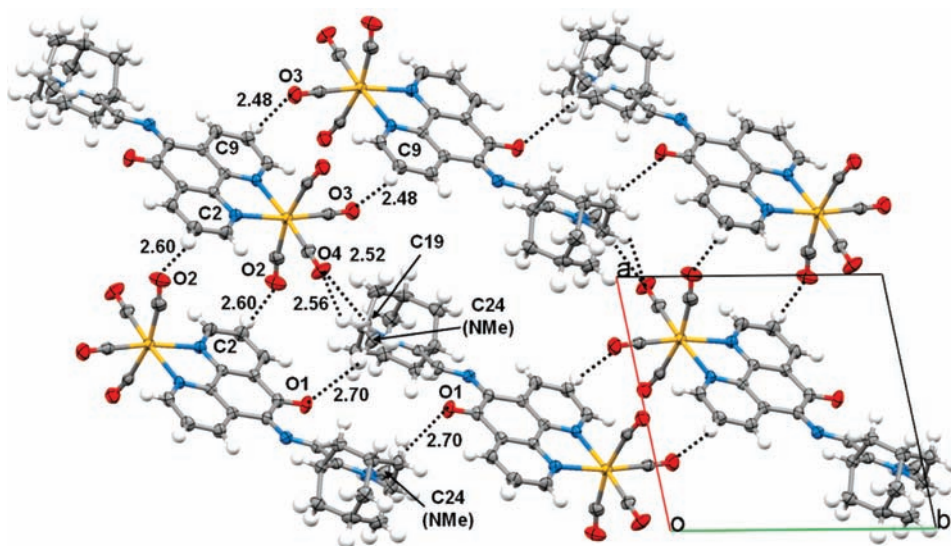
Figure 7. Molecular packing of **3**-PMC shown along the *c* axis, illustrating the interaction network. Toluene solvate molecules are omitted for clarity.
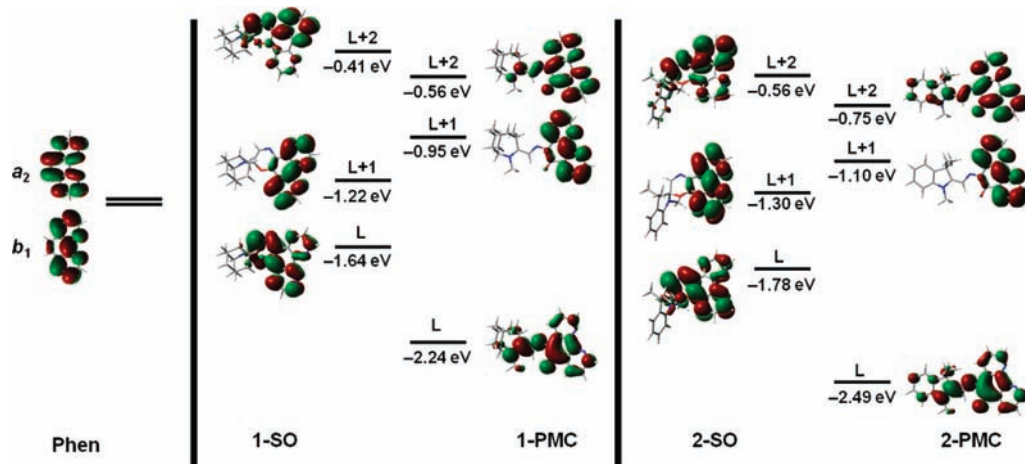

Figure 8. Lowest-lying molecular orbitals of phen (left) and the SO and PMC forms of **1** (center) and **2** (right) calculated using DFT at the B3LYP/6-31G(d,p) level of theory (isovalues: MO = 0.02, density = 0.0004).

Upon structural change from the SO to the PMC form in **1** and **2**, the LUMO and LUMO+2 orbitals are stabilized by ~0.6 and 0.2 eV, respectively, while the LUMO+1 is destabilized by ~0.2 eV. In the PMC form of the ligands, both the orbital populations of the LUMO and LUMO+2 change significantly such that, while the LUMO has predominantly oxazine character, the LUMO+2 has predominantly phen(a_2) character. The MOs of the azahomoadamantyl and indolyl derivatives **1** and **2** are nearly identical, although the MOs of **2** are slightly lower in energy than those of **1** and exhibit in some cases a greater delocalization of electron density onto the indolyl moiety. Thus, the nature and magnitude of ligand field effects upon photoisomerization of **1** and **2** critically depend on whether mixing occurs between the metal orbitals and the a_2-symmetric LUMO/LUMO+2 pair or the b_1-symmetric LUMO+1 orbital.

The relative energies of the SO and PMC LUMOs for both **1** and **2** correlate well with their relative reduction potentials, even though these values are derived from gas- and solution-phase data, respectively. The energy difference between the reduction processes assigned for **1**-PMC and **2**-SO $[E_{pc(Red1,1)} - E_{pc(Red2,2)} = 0.44$ V in CH_3CN and 0.49 V in $CH_2Cl_2]$ correlates remarkably well with the energy difference between the corresponding LUMOs $[E_{LUMO(2\text{-}SO)} - E_{LUMO(1\text{-}PMC)} = 0.46$ eV$]$. The difference between the first and second cathodic peak potentials for **2**, assigned tentatively to the PMC and SO forms, respectively $[E_{pc(Red1,2)} - E_{pc(Red2,2)} = 0.69$ V in CH_3CN and 0.80 V in $CH_2Cl_2]$, also correlates well with the energy difference between the corresponding LUMOs $[E_{LUMO(2\text{-}SO)} - E_{LUMO(2\text{-}PMC)} = 0.71$ eV$]$.

$M(CO)_x(L)_y$ complexes (M = Mo, Cr, W) are useful probes of ligand (L) bonding properties because of the sensitivity of the carbonyl groups to their electronic environment.[21] Metal—carbonyl bonding can be qualitatively described by a synergistic bonding model whereby the CO group transfers electron density to the metal through σ-donation and the metal transfers electron density to the carbonyl group through π-backbonding. Ancillary ligand(s), L, will compete with the CO groups in the transfer of electron density to and from the metal center as a function of
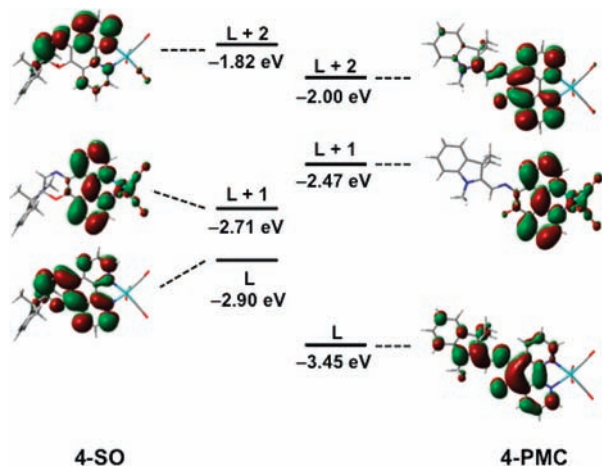
10090

dx.doi.org/10.1021/ja109776z |*J. Am. Chem. Soc.* 2011, 133, 10081–10093

Figure 9. Lowest-lying molecular orbitals of the SO and PMC forms of **4** calculated using DFT at the B3LYP/LANL2DZ level of theory (isovalues: MO = 0.02, density = 0.0004).

their σ-donor or π-acceptor abilities. In order to assess changes in electronic structure at the metal center upon photoisomerization, geometry optimizations were performed on the Mo complexes using the double-ζ effective core potential LANL2DZ basis set.[35,52] The B3LYP/LANL2DZ level of theory has been used successfully in the analysis of frontier MO schemes for $M(CO)_4$-(NN) (M = Cr, Mo, W; NN = diimine) complexes.[53] The optimized geometry of **3**-PMC is in satisfactory agreement with the crystal structure of this complex, with bond lengths deviating by up to 0.04 Å between the two. Molecular orbitals obtained from a single-point energy calculation using the experimental geometry for **3**-PMC predict a reversal in the ordering of the very close-lying HOMO−2 and HOMO−1 orbitals. For **3**-SO, we were unable to obtain a minimized geometry in which the C_{spiro}−O bond remained intact. The instability of this bond is consistent with the long C_{spiro}−O bond lengths typically found in spiropyrans and spirooxazines[48b,54] and the exceptional stability of the PMC form of this particular compound (vide supra). The MO schemes obtained for the SO and PMC forms of **4** were therefore used for the bonding analysis.

The frontier MOs of $Mo(CO)_4(APSO)$ (**4**) are shown in Figure 9. The three highest occupied MOs are virtually identical for both the SO and PMC forms of the complex and have predominantly $Mo(CO)_4$ character, with some orbital population on the spirooxazine ligand (SI). The three lowest unoccupied MOs have predominantly ligand π* character, with electron density distributions and relative energies similar to those of the free ligands. The LUMO+1 MOs also have some $Mo(CO)_4$ orbital character in both the SO and PMC forms of the complexes.

The bonding in $Mo(CO)_4$−spirooxazine complexes can be analyzed within the context of a fragment molecular orbital approach analogous to that of the parent $Mo(CO)_4(phen)$ complex. In $Mo(CO)_4(phen)$, the $Mo(CO)_4$ fragment, under C_{2v} symmetry constraints, has three filled frontier MOs of b_1, a_2, and a_1 symmetries, which possess a mixture of predominantly CO π* character and metal d_{xz}, d_{xy}, and $d_{z^2}/d_{x^2−y^2}$ characters, respectively, and two unoccupied frontier MOs of b_2 and a_1 symmetries.[55] Phenanthroline possesses two low-lying unoccupied π* orbitals of b_1 and a_2 symmetries with nearly equal energies (Figure 8). These orbitals are of the correct symmetry to mix with the filled $Mo(CO)_4$ group orbitals of b_1 symmetry (with

predominantly d_{xz} character) and a_2 symmetry (with predominantly d_{xy} character) (SI). Greater mixing between $Mo(CO)_4$ (b_1, d_{xz}) and phen (b_1, π*) relative to $Mo(CO)_4$ (a_2, d_{xy}) and phen (a_2, π*) occurs,[50,56] and the former interaction represents the primary pathway for Mo (d)→phen (π*) backbonding.

The above analysis can be extended to the SO and PMC forms of the Mo−tetracarbonyl spirooxazine complexes, for which pseudo-C_{2v} symmetry is assumed in order to approximate the bonding interactions. In the MOs of both the SO and PMC forms (Figure 9), it is evident that the greatest phen (π*)−$Mo(CO)_4$ (d) mixing occurs between the fragment MOs of b_1 symmetry. In the three highest occupied MOs, phen (π*) mixing is observed to a moderate degree in the metal-based b_1-symmetry $Mo(CO)_4$ (d) HOMO−2, to a small degree in the a_2-symmetry $Mo(CO)_4$ (d) HOMO−1, and to a very small degree in the a_1-symmetry $Mo(CO)_4$ (d) HOMO (SI). In the three lowest unoccupied MOs, a significant amount of $Mo(CO)_4$ (d) mixing is observed in the ligand-based pseudo-b_1-symmetry phen (π*) LUMO+1, no $Mo(CO)_4$ (d) mixing is observed in the pseudo-a_2-symmetry phen (π*) LUMO, and only a very small amount of $Mo(CO)_4$ (d) mixing is observed in the pseudo-a_2-symmetry phen (π*) LUMO+2. The relative molecular orbital contributions from the $Mo(CO)_4$ fragment and the ligand fragment thus parallel those described above for the $M(CO)_4(phen)$ complexes (see SI).

Most critical to the analysis are the differences between the SO and PMC ligands. Since the mixing between ligand and metal MOs of b_1 symmetry is primarily responsible for the Mo (d)→phen (π*) backbonding interaction, the LUMO+1 should be most important in determining the ligand field strength of the PMC and SO forms of the spirooxazines. Because this MO is lower in energy in the SO form than in the PMC form (by 0.20 eV for **3** and 0.27 eV for **4**), the SO form is expected to be a stronger π-acceptor. Contributions from metal−ligand mixing of the a_2-symmetry MOs should have the same effect on the relative SO and PMC π-acceptor strengths as the a_2-symmetry LUMO of the SO form is significantly lower in energy than the a_2-symmetry LUMO+2 of the PMC form. The LUMO of the PMC form, despite being lowest in energy, has no orbital population on the phenanthroline nitrogen atoms and would not be expected to contribute significantly to metal−ligand bonding. Overall, the conclusions from the DFT MO analysis with regard to the bonding properties of the SO and PMC forms of the spirooxazine ligands are consistent with the experimental FT-IR and ^{13}C NMR results.

The azahomoadamantyl and indolyl spirooxazine ligands **1** and **2** display very similar frontier MOs, which suggests that while spirooxazine derivatization of phen leads to significant changes to the phen-based MOs upon SO/PMC isomerization, the specific type of spirooxazine functionality does not contribute significantly to the overall nature of these changes. The type of spirooxazine does slightly influence the absolute energies of the MOs, however, and could be exploited to tune metal−ligand orbital matching. Of the three lowest unoccupied MOs, the LUMO+1 plays the most significant role in Mo (d)→phen (π*) backbonding. The relative energy of this orbital cannot be easily probed experimentally through electrochemical studies, as would be expected for the LUMO, and it can therefore be more readily studied computationally. The difference in MO electron density distribution and/or energy between the SO and PMC forms is more pronounced for the LUMO and LUMO+2 than the LUMO+1. This is likely due to the degree of spirooxazine−phen fragment MO mixing, which is expected to be greater for the

a_2-symmetry phen orbitals with more electron density at the 5- and 6-positions.

CONCLUSIONS

We have developed a generalized and powerful method for evaluating both the direction and magnitude of ligand field changes associated with photoisomerization of photochromic organic metal complexes and the effect of photoisomerization on a bound metal center. Spectroscopic investigation of photochromic metal—carbonyl complexes by FT-IR and ^{13}C NMR spectroscopies, coupled with structural and computational analysis, has been found to provide an effective strategy for experimentally quantifying and assessing electronic structure changes in photochromic ligands as optical components in smart materials. The methodology was successfully applied here to the analysis of phenanthroline—spirooxazine ligands. A change in ligand field strength between the SO and PMC forms was demonstrated through FT-IR and ^{13}C NMR analysis of the Mo complexes, where both analyses are consistent with the SO form as a stronger π-acceptor. DFT fragment molecular orbital analysis showed that, of the low-lying unoccupied MOs of the ligands, the LUMO+1, a pseudo-b_1-symmetry phen-based π^* MO, exhibits the greatest amount of mixing with the $Mo(CO)_4$ fragment and is therefore primarily responsible for the Mo (d)→phen (π^*) backbonding interaction. In the spirooxazine derivatives, the LUMO+1 is 0.2−0.3 eV lower in the SO form than in the PMC form, which implies that the SO form is a stronger π-acceptor, consistent with the FT-IR and ^{13}C NMR experimental results.

As analogous metal—ligand bonding interactions would be expected for a wide range of metals with photochromic phenanthroline-based ligands, the MO analysis provided here allows prediction of the optical switching of ligand field around the metal for tuning of metal-based electronic states. Utilizing molybdenum—carbonyl complexes to evaluate the changes in ligand field effects can therefore be expanded to evaluation of a wide variety of photochromic ligands. Finally, the unambiguous changes upon photoisomerization observed in metal center electronic structure highlight the potential for designing switchable smart materials based on hybrid inorganic—organic coordination complexes of photochromes. This may be a powerful approach for introducing optical modulation of metal-based properties, either directly through ligand field effects or indirectly through modulation of orbital energies.

ASSOCIATED CONTENT

S **Supporting Information.** Full characterization data for **3** and **4**; electronic absorption spectroscopy details and TD-DFT calculation results; ^{1}H and ^{13}C NMR spectra of **3** and **4**; ^{1}H NMR spectra of **3** in DMSO-d_6 over time; solution-state behavior of **4** in toluene and CH_2Cl_2 monitored by UV/vis electronic absorption spectroscopy; CVs of **1**, **2**, and **3** in CH_2Cl_2; FT-IR sample cell of **3** upon visible irradiation; FT-IR spectra of **3** in Nujol and KBr upon visible irradiation; additional MO schemes for **1**, **2**, and **4**; $Mo(CO)_4$(phen) MO analysis; Gaussian calculation outputs; full ref 31; CIF file for **3**-PMC. This material is available free of charge via the Internet at http://pubs.acs.org.

AUTHOR INFORMATION

Corresponding Author

nlfrank@uvic.ca

REFERENCES

(1) (a) Kawata, S.; Kawata, Y. Chem. Rev. **2000**, 100, 1777–1788. (b) Irie, M. Chem. Rev. **2000**, 100, 1685–1716. (c) Yokoyama, Y. Chem. Rev. **2000**, 100, 1717–1739. (d) Berkovic, G.; Krongauz, V.; Weiss, V. Chem. Rev. **2000**, 100, 1741–1753. (e) Gust, D.; Moore, T. A.; Moore, A. L. Chem. Commun. **2006**, 1169–1178. (f) de Silva, A. P.; McClenaghan, N. D. Chem.—Eur. J. **2004**, 10, 574–586.

(2) (a) Joachim, C.; Gimzewski, J. K.; Aviram, A. Nature **2000**, 408, 541–548. (b) Sheats, J. R.; Barbara, P. F. Acc. Chem. Res. **1999**, 32, 191–192. (c) Willner, I. Acc. Chem. Res. **1997**, 30, 347–356.

(3) Browne, W. R.; Feringa, B. L. Annu. Rev. Phys. Chem. **2009**, 60, 407–428.

(4) Lendlein, A.; Jiang, H. Y.; Junger, O.; Langer, R. Nature **2005**, 434, 879–882.

(5) Lowik, D.; Leunissen, E. H. P.; van den Heuvel, M.; Hansen, M. B.; van Hest, J. C. M. Chem. Soc. Rev. **2010**, 39, 3394–3412.

(6) Movia, D.; Prina-Mello, A.; Volkov, Y.; Giordani, S. Chem. Res. Toxicol. **2010**, 23, 1459–1466.

(7) (a) Ballardini, R.; Balzani, V.; Credi, A.; Gandolfi, M. T.; Venturi, M. Acc. Chem. Res. **2001**, 34, 445–455. (b) Zhou, M. G.; Liang, X. G.; Mochizuki, T.; Asanuma, H. Angew. Chem., Int. Ed. **2010**, 49, 2167–2170.

(8) (a) Crano, J. C.; Guglielmetti, R. J. Organic Photochromic and Thermochromic Compounds; Kluwer Academic Publishers: New York, 2002; Vols. 1 and 2. (b) Dürr, H.; Bouas-Laurent, H. Photochromism: Molecules and Systems; Elsevier: New York, 2003. (c) Brown, H. G. Photochromism; Wiley-Interscience: New York, 1971; Vol. III.

(9) (a) Akita, M. Organometallics **2011**, 30, 43–51. (b) Wong, H. L.; Tao, C. H.; Zhu, N. Y.; Yam, V. W. W. Inorg. Chem. **2011**, 50, 471–481. (c) Tissot, A.; Boillot, M. L.; Pillet, S.; Codjovi, E.; Boukheddaden, K.; Daku, L. M. L. J. Phys. Chem. C **2010**, 114, 21715–21722. (d) Li, X.; Zhang, Q.; Tu, Y. Q.; Agren, H.; Tian, H. Phys. Chem. Chem. Phys. **2010**, 12, 13730–13736. (e) Guerchais, V.; Ordronneau, L.; Le Bozec, H. Coord. Chem. Rev. **2010**, 254, 2533–2545. (f) Nakai, H.; Isobe, K. Coord. Chem. Rev. **2010**, 254, 2652–2662. (g) Natali, M.; Soldi, L.; Giordani, S. Tetrahedron **2010**, 66, 7612–7617. (h) Ohkoshi, S.; Tsunobuchi, Y.; Matsuda, T.; Hashimoto, K.; Namai, A.; Hakoe, F.; Tokoro, H. Nature Chem. **2010**, 2, 539–545. (i) Browne, W. R.; Feringa, B. L. Chimia **2010**, 64, 398–403. (j) Tanaka, Y.; Ishisaka, T.; Inagaki, A.; Koike, T.; Lapinte, C.; Akita, M. Chem.—Eur. J. **2010**, 16, 4762–4776. (k) Ko, C. C.; Yam, V. W. W. J. Mater. Chem. **2010**, 20, 2063–2070. (l) Wang, M. S.; Xu, G.; Zhang, Z. J.; Guo, G. C. Chem. Commun. **2010**, 46, 361–376. (m) Dong, B. X.; Xu, Q. Inorg. Chem. **2009**, 48, 5861–5873. (n) Zhong, Y. W.; Vila, N.; Henderson, J. C.; Abruna, H. D. Inorg. Chem. **2009**, 48, 991–999. (o) Kojima, N.; Okubo, M.; Shimizu, H.; Enomoto, M. Coord. Chem. Rev. **2007**, 251, 2665–2673. (p) Tian, H.; Feng, Y. L. J. Mater. Chem. **2008**, 18, 1617–1622. (q) Nishimura, G.; Maehara, H.; Shiraishi, Y.; Hirai, T. Chem.—Eur. J. **2008**, 14, 259–271. (r) Zhong, Y. W.; Vila, N.; Henderson, J. C.; Flores-Torres, S.; Abruna, H. D. Inorg. Chem. **2007**, 46, 10470–10472. (s) Lee, P. H. M.; Ko, C. C.; Zhu, N. Y.; Yam, V. W. W. J. Am. Chem. Soc. **2007**, 129, 6058. (t) Belser, P.; De Cola, L.; Hartl, F.; Adamo, V.; Bozic, B.; Chriqui, Y.; Iyer, V. M.; Jukes, R. T. F.; Kuhni, J.; Querol, M.; Roma, S.; Salluce, N. Adv. Funct. Mater. **2006**, 16, 195–208. (u) Kume, S.; Nishihara, H. Dalton Trans. **2008**, 3260–3271.

(10) (a) Tanaka, Y.; Inagaki, A.; Akita, M. Chem. Commun. **2007**, 1169–1171. (b) Takayama, K.; Matsuda, K.; Irie, M. Chem.— Eur. J. **2003**, 9, 5605–5609.

(11) (a) Jukes, R. T. F.; Adamo, V.; Hartl, F.; Belser, P.; De Cola, L. *Inorg. Chem.* **2004**, *43*, 2779–2792. (b) Ngan, T. W.; Ko, C. C.; Zhu, N. Y.; Yam, V. W. W. *Inorg. Chem.* **2007**, *46*, 1144–1152.

(12) (a) Cacciapaglia, R.; Di Stefano, S.; Mandolini, L. *J. Am. Chem. Soc.* **2003**, *125*, 2224–2227. (b) Samachetty, H. D.; Branda, N. R. *Chem. Commun.* **2005**, 2840–2842. (c) Winkler, J. D.; Bowen, C. M.; Michelet, V. *J. Am. Chem. Soc.* **1998**, *120*, 3237–3242.

(13) Paquette, M. M.; Kopelman, R. A.; Beitler, E.; Frank, N. L. *Chem. Commun.* **2009**, 5424–5426.

(14) (a) Roux, C.; Zarembowitch, J.; Gallois, B.; Granier, T.; Claude, R. *Inorg. Chem.* **1994**, *33*, 2273–2279. (b) Senechal-David, K.; Zaman, N.; Walko, M.; Halza, E.; Riviere, E.; Guillot, R.; Feringa, B. L.; Boillot, M. L. *Dalton Trans.* **2008**, 1932–1936. (c) Boillot, M. L.; Pillet, S.; Tissot, A.; Riviere, E.; Claiser, N.; Lecomte, C. *Inorg. Chem.* **2009**, *48*, 4729–4736.

(15) Nakagawa, T.; Hasegawa, Y.; Kawai, T. *Chem. Commun.* **2009**, 5630–5632.

(16) Minkin, V. I. *Chem. Rev.* **2004**, *104*, 2751–2776.

(17) Patel, D. G.; Paquette, M. M.; Kopelman, R. A.; Kaminsky, W.; Ferguson, M. J.; Frank, N. L. *J. Am. Chem. Soc.* **2010**, *132*, 12568–12586.

(18) Kopelman, R. A.; Snyder, S. M.; Frank, N. L. *J. Am. Chem. Soc.* **2003**, *125*, 13684–13685.

(19) Kopelman, R. A.; Paquette, M. M.; Frank, N. L. *Inorg. Chim. Acta* **2008**, *361*, 3570–3576.

(20) (a) Hasegawa, Y.; Nakagawa, T.; Kawai, T. *Coord. Chem. Rev.* **2010**, *254*, 2643–2651. (b) Peter, B. *Chimia* **2010**, *64*, 356–361.

(21) (a) Graham, W. A. G. *Inorg. Chem.* **1968**, *7*, 315–321. (b) Hocking, R. K.; Hambley, T. W. *Organometallics* **2007**, *26*, 2815–2823. (c) Tolman, C. A. *J. Am. Chem. Soc.* **1970**, *92*, 2953–2956. (d) Barbeau, C.; Turcotte, J. *Can. J. Chem.* **1976**, *54*, 1603–1611.

(22) Bao, D. D.; Millare, B.; Xia, W.; Steyer, B. G.; Gerasimenko, A. A.; Ferreira, A.; Contreras, A.; Vullev, V. I. *J. Phys. Chem. A* **2009**, *113*, 1259–1267.

(23) *SAINT*, Version 7.53A; Bruker AXS Inc.: Madison, WI, 1997−2008.

(24) *SADABS*, Version 2008/1; Bruker AXS Inc.: Madison, WI, 2008.

(25) Altomare, A.; Burla, M. C.; Camalli, M.; Cascarano, G. L.; Giacovazzo, C.; Guagliardi, A.; Moliterni, A. G. G.; Polidori, G.; Spagna, R. *J. Appl. Crystallogr.* **1999**, *32*, 115–119.

(26) Cromer, D. T.; Waber, J. T. *International Tables for X-Ray Crystallography*; The Kynoch Press: England, 1974; Vol. IV.

(27) Ibers, J. A.; Hamilton, W. C. *Acta Crystallogr.* **1964**, *17*, 781–782.

(28) Creagh, D. C.; McAuley, W. J. In *International Tables for Crystallography*; Wilson, A. J. C., Ed.; Kluwer Academic Publishers: Boston, 1992; Vol. C, pp 219−222.

(29) Creagh, D. C.; Hubbell, J. H. In *International Tables for Crystallography*; Wilson, A. J. C., Ed.; Kluwer Academic Publishers: Boston, 1992; Vol. C, pp 200−206.

(30) *SHELXTL*, Version 5.1; Bruker AXS Inc.: Madison, WI, 1997.

(31) Frisch, M. J.; et al. *Gaussian 03*, Revision E.01; Gaussian Inc.: Wallingford, CT, 2004.

(32) Ziegler, T. *Chem. Rev.* **1991**, *91*, 651–667.

(33) Becke, A. D. *J. Chem. Phys.* **1993**, *98*, 5648–5652.

(34) Lee, C. T.; Yang, W. T.; Parr, R. G. *Phys. Rev. B* **1988**, *37*, 785–789.

(35) (a) Hay, P. J.; Wadt, W. R. *J. Chem. Phys.* **1985**, *82*, 299–310. (b) Wadt, W. R.; Hay, P. J. *J. Chem. Phys.* **1985**, *82*, 284–298.

(36) Darensbourg, D. J.; Kump, R. L. *Inorg. Chem.* **1978**, *17*, 2680–2682.

(37) Mishra, A.; Behera, R. K.; Behera, P. K.; Mishra, B. K.; Behera, G. B. *Chem. Rev.* **2000**, *100*, 1973–2011.

(38) It should be noted that because the MLCT and PMC $\pi-\pi^*$ absorption bands overlap in the Mo complexes, the reported λ_{max} and ε_{PMC} values may be slightly different than expected for the isolated $\pi-\pi^*$ and MLCT transitions.

(39) Metelitsa, A. V.; Micheau, J. C.; Voloshin, N. A.; Voloshina, E. N.; Minkin, V. I. *J. Phys. Chem. A* **2001**, *105*, 8417–8422.

(40) Bard, A. J.; Faulkner, L. R. *Electrochemical Methods—Fundamentals and Applications*, 2nd ed.; John Wiley & Sons: Toronto, 2001.

(41) ^{1}H NMR spectra of **1** in CD$_3$CN and CD$_2$Cl$_2$ with 0.1 M TBA-TFB confirmed that the presence of the electrolyte does not lead to a shift in the $K =$ [SO]/[PMC] equilibrium constant.

(42) Kraihanzel, C. A.; Cotton, F. A. *Inorg. Chem.* **1963**, *2*, 533–540.

(43) (a) Cotton, F. A.; Kraihanz.Cs *J. Am. Chem. Soc.* **1962**, *84*, 4432–4438. (b) Cotton, F. A. *Inorg. Chem.* **1964**, *3*, 702–711.

(44) (a) Ernst, S.; Kaim, W. *J. Am. Chem. Soc.* **1986**, *108*, 3578–3586. (b) Shiu, K. B.; Wang, S. L.; Liao, F. L. *J. Organomet. Chem.* **1991**, *420*, 207–215. (c) Manuta, D. M.; Lees, A. J. *Inorg. Chem.* **1986**, *25*, 1354–1359. (d) Hutchinson, B.; Nakamoto, K. *Inorg. Chim. Acta* **1969**, *3*, 591–595. (e) Clauti, G.; Zassinovich, G.; Mestroni, G. *Inorg. Chim. Acta* **1986**, *112*, 103–106. (f) Kulasingham, G. C.; McWhinnie, W. R. *J. Less-Common Met.* **1966**, *10*, 72–74.

(45) (a) Gansow, O. A.; Kimura, B. Y.; Dobson, G. R.; Brown, R. A. *J. Am. Chem. Soc.* **1971**, *93*, 5922–5924. (b) Mann, B. E. *J. Chem. Soc., Dalton Trans.* **1973**, 2012–2015.

(46) Allen, F. H.; Kennard, O.; Watson, D. G.; Brammer, L.; Orpen, A. G.; Taylor, R. *J. Chem. Soc., Perkin Trans. 2* **1987**, S1–S19.

(47) Bruins Slot, H. J.; Murrall, N. W.; Welch, A. J. *Acta Crystallogr. Sect. C: Cryst. Struct. Commun.* **1985**, *41*, 1309–1312.

(48) (a) Perrier, A.; Maurel, F.; Perpete, E. A.; Wathelet, V.; Jacquemin, D. *J. Phys. Chem. A* **2009**, *113*, 13004–13012. (b) Aldoshin, S. *Russ. Chem. Rev.* **1990**, *59*, 663–685. (c) Lareginie, P.; Lokshin, V.; Samat, A.; Guglielmetti, R.; Pepe, G. *J. Chem. Soc., Perkin Trans. 2* **1996**, 107–111. (d) Song, H. F.; Chen, K. C.; Tian, H. *Dyes Pigm.* **2005**, *67*, 1–7. (e) Nakamura, S.; Uchida, K.; Murakami, A.; Irie, M. *J. Org. Chem.* **1993**, *58*, 5543–5545.

(49) (a) Minkin, V. I.; Metelitsa, A. V.; Dorogan, I. V.; Lukyanov, B. S.; Besugliy, S. O.; Micheau, J. C. *J. Phys. Chem. A* **2005**, *109*, 9605–9616. (b) Maurel, F.; Aubard, J.; Rajzmann, M.; Guglielmetti, R.; Samat, A. *J. Chem. Soc., Perkin Trans. 2* **2002**, 1307–1315. (c) Sheng, Y. H.; Leszczynski, J.; Garcia, A. A.; Rosario, R.; Gust, D.; Springer, J. *J. Phys. Chem. B* **2004**, *108*, 16233–16243.

(50) Ernst, S.; Vogler, C.; Klein, A.; Kaim, W.; Zalis, S. *Inorg. Chem.* **1996**, *35*, 1295–1300.

(51) Klein, A.; Kaim, W.; Waldhor, E.; Hausen, H. D. *J. Chem. Soc., Perkin Trans. 2* **1995**, 2121–2126.

(52) Hay, P. J.; Wadt, W. R. *J. Chem. Phys.* **1985**, *82*, 270–283.

(53) (a) Makedonas, C.; Mitsopoulou, C. A. *Eur. J. Inorg. Chem.* **2007**, 110–119. (b) Yang, L.; Feng, J. K.; Ren, A. M. *Synth. Met.* **2005**, *152*, 265–268.

(54) Aldoshin, S. M.; Chuev, I. I.; Filipenko, O. S.; Utenyshev, A. N.; Lokshin, V.; Laregenie, P.; Samat, A.; Guglielmetti, R. *Russ. Chem. Bull.* **1998**, *47*, 1089–1097.

(55) Elian, M.; Hoffmann, R. *Inorg. Chem.* **1975**, *14*, 1058–1076.

(56) Richardson, D. E. *J. Chem. Educ.* **1993**, *70*, 372–380.